Statistical Study of EMIC Waves and Related Proton Distributions Observed by the Arase Satellite

Chae-Woo Jun[1], Yoshizumi Miyoshi[1], Satoko Nakamura[1], Masafumi Shoji[2], Masahiro Kitahara[3], Tomoaki Hori[1], Chao Yue[4], Jacob Bortnik[5], Larry R. Lyons[5], Kyungguk Min[6], Yoshiya Kasahara[7], Fuminori Tsuchiya[3], Atsushi Kumamoto[3], Kazushi Asamura[8], Iku Shinohara[9], Ayako Matsuoka[10], Shun Imajo[10], Shoichiro Yokota[11], Satoshi Kasahara[12], and Kunihiro Keika[12]

[1]Institute for Space-Earth Environmental Research, Nagoya University
[2]Nagoya University
[3]Tohoku University
[4]Peking Univeristy
[5]University of California Los Angeles
[6]Chungnam National University
[7]Kanazawa University
[8]The Institute of Space and Astronautical Science
[9]Japan Aerospace Exploration Agency
[10]Kyoto University
[11]Osaka University
[12]The University of Tokyo

December 7, 2022

Abstract

We performed a statistical study of electromagnetic ion cyclotron (EMIC) wave distributions and their coupling with energetic protons in the inner magnetosphere using the Arase satellite data from May 2017 to December 2020. We investigated the energetic proton pitch-angle distributions and partial thermal pressures associated with EMIC waves using inter-calibrated proton data in the energy range of 30 eV/q-187 keV/q. With a cold plasma approximation, we computed the proton minimum resonance energies using the observed EMIC wave frequency and plasma density values. We found that the EMIC waves had left-handed polarization near the magnetic equator close to the threshold of proton cyclotron instability, and propagated to higher latitudes along the field line with polarization reversal. H-EMIC waves showed two peak occurrence regions in the morning and noon sectors at L=7.5-9 outside the plasmasphere. The flux enhancements associated with morning side H-EMIC waves appeared at E<1 keV/q among all pitch angles, while H-EMIC waves in the noon sector exhibited flux enhancement in field-aligned directions at E=1-100 keV/q. He-EMIC waves showed a broad occurrence region from 12 to 20 magnetic local time at L=5.5-8.5 inside the plasmasphere with strong flux enhancements at all pitch-angle ranges at E=1-100 keV/q. The proton minimum resonance energy using the obtained central frequency was consistent with the observed flux enhancements at different peak occurrence regions. We conclude that the free energy sources of EMIC waves in different geomagnetic environments drive the two different types of EMIC waves, and they interact with energetic protons at different energy ranges.

1 **Statistical Study of EMIC Waves and Related Proton Distributions Observed by the**
2 **Arase Satellite**

3 **C.-W. Jun[1], Y. Miyoshi[1], S. Nakamura[1], M. Shoji[1], M. Kitahara[1], T. Hori[1], C. Yue[2], J.**
4 **Bortnik[3], L. Lyons[3], K. Min[4], Y. Kasahara[5], F. Tsuchiya[6], A. Kumamoto[6], K. Asamura[7], I.**
5 **Shinohara[7], A. Matsuoka[8], S. Imajo[8], S. Yokota[9], S. Kasahara[10], and K. Keika[10]**

6 [1]Institute for Space-Earth Environmental Research (ISEE), Nagoya University, Nagoya, Japan

7 [2]Institute of Space Physics and Applied Technology, Peking University, Beijing, China

8 [3]AOS/UCLA, Los Angeles, USA

9 [4]Chungnam National University, Daejeon, Korea

10 [5]Kanazawa University, Kanazawa, Japan

11 [6]Tohoku University, Sendai, Japan

12 [7]ISAS/JAXA, Tokyo, Japan

13 [8]Kyoto University, Kyoto, Japan

14 [9]Osaka University, Osaka, Japan

15 [10]University of Tokyo, Tokyo, Japan

16

17 Corresponding author: Chae-Woo Jun (chae-woo@isee.nagoya-u.ac.jp)

18

19 **Key Points:**

20 • H- (He-) EMIC waves are observed in the morning-noon (afternoon) sector outside (inside)
21 the plasmasphere.

22 • EMIC waves are generated at the magnetic equator near the threshold of proton cyclotron
23 instability and propagate to higher latitudes.

24 • The energy ranges of the observed proton pitch angle scatter differ in different occurrence
25 regions, and coincide with the resonance energy using the central EMIC wave frequency.

26 **Abstract**

27 We performed a statistical study of electromagnetic ion cyclotron (EMIC) wave distributions and
28 their coupling with energetic protons in the inner magnetosphere using the Arase satellite data
29 from May 2017 to December 2020. We investigated the energetic proton pitch-angle distributions
30 and partial thermal pressures associated with EMIC waves using inter-calibrated proton data in the
31 energy range of 30 eV/q-187 keV/q. With a cold plasma approximation, we computed the proton
32 minimum resonance energies using the observed EMIC wave frequency and plasma density
33 values. We found that the EMIC waves had left-handed polarization near the magnetic equator
34 close to the threshold of proton cyclotron instability, and propagated to higher latitudes along the
35 field line with polarization reversal. H-EMIC waves showed two peak occurrence regions in the
36 morning and noon sectors at L = 7.5-9 outside the plasmasphere. The flux enhancements associated
37 with morning side H-EMIC waves appeared at E < 1 keV/q among all pitch angles, while H-EMIC
38 waves in the noon sector exhibited flux enhancement in field-aligned directions at E = 1-100
39 keV/q. He-EMIC waves showed a broad occurrence region from 12 to 20 magnetic local time at
40 L = 5.5-8.5 inside the plasmasphere with strong flux enhancements at all pitch-angle ranges at E
41 = 1-100 keV/q. The proton minimum resonance energy using the obtained central frequency was
42 consistent with the observed flux enhancements at different peak occurrence regions. We conclude
43 that the free energy sources of EMIC waves in different geomagnetic environments drive various
44 types of EMIC waves, and they interact with energetic protons at different energy ranges.

45

46 **Plain Language Summary**
47 Electromagnetic ion cyclotron (EMIC) waves are considered to play an important role in
48 controlling magnetospheric plasma dynamics. Specifically, EMIC wave-particle interactions can
49 cause the loss of energetic protons and relativistic electrons in the Earth's magnetosphere, and the
50 scattered particles precipitate into the ionosphere, creating isolated proton auroras at sub-auroral
51 latitudes (55-65 geomagnetic latitudes). To understand the coupling of EMIC waves with energetic
52 protons in the inner magnetosphere, we performed a statistical study of proton distributions
53 associated with EMIC waves using a 4-year in-situ observation obtained by the Arase satellite. We
54 observed dawn-dusk asymmetric EMIC wave distributions depending on the wavebands. We also
55 found three significantly different regions of EMIC waves showing different characteristics. EMIC
56 waves were inferred to be generated near the magnetic equator and propagate to higher magnetic
57 latitudes along the field line. Furthermore, EMIC waves in different regions were proposed to
58 interact with energetic protons at different energy ranges. The Arase satellite observations used in
59 this study provided new insights into the dynamics of EMIC waves in the inner magnetosphere.

1 Introduction

Earth's magnetosphere consists of various plasma populations at varying energy and plasma density conditions (Borovsky and Valdivia, 2018). The plasmasphere consists of the densest ($> 100/cm^3$) and coldest (< 1 eV) plasma within the range of 1-4 R_E. The ring current region has a torus-like structure with the highest energy density in the inner magnetosphere (Kanekal and Miyoshi, 2021). During disturbed geomagnetic conditions, energetic plasma is transported from the magnetotail to the magnetosphere, contributing to various plasma distributions in the inner magnetosphere. This causes different types of instabilities in the generation of various plasma waves (e.g., Thorne, 2010; Miyoshi et al., 2018a).

Electromagnetic Ion Cyclotron (EMIC) waves are one of the magnetospheric plasma waves that play an important role in the loss of energetic protons and sub-relativistic, relativistic, and ultra-relativistic electrons in the outer radiation belts due to pitch-angle scattering by wave-particle interactions (Thorne, 2010; Kurita et al., 2018; Li and Hudson, 2019; Miyoshi et al., 2022). The protons scattered by EMIC wave-particle interactions precipitate into the ionosphere, causing isolated proton auroras (IPAs) at sub-auroral latitudes (55-65 geomagnetic latitudes) (Sakaguchi et al., 2007; Ozaki et al., 2018, 2021) and relativistic electrons simultaneously precipitate inside IPAs (Miyoshi et al., 2008; Shumko et al., 2022).

EMIC waves have left-handed (LH) polarizations near the wave source regions in the frequency range below the proton gyrofrequency. Because of the existence of heavy ions, the EMIC wave branch can be divided into three regimes in the dispersion relation: H-band EMIC waves, hereafter referred to as H-EMIC waves, between the proton (f_{cH}) and helium (f_{cHe}) gyrofrequencies; He-band EMIC waves, hereafter referred to as He-EMIC waves, between f_{cHe} and oxygen gyrofrequency (f_{cO}); and O-EMIC waves below f_{cO} (e.g., Kozyra et al., 1984; Chen et al., 2010).

An inverse relationship between the temperature anisotropy ($T_{\perp,p}/T_{\parallel,p}$) and parallel proton plasma beta ($\beta_{\parallel,p}$) for the proton-electron system can be derived as:

$$\frac{T_\perp}{T_\parallel} = 1 + \frac{a}{\beta_\parallel^b} \quad (1)$$

where the parameters a and b are obtained as functions of the ratio between the hot and cold proton densities. Here, $T_{\perp,p}$ and $T_{\parallel,p}$ are the perpendicular and parallel components of the proton temperature to the ambient magnetic field, $\beta_{\parallel,p} = 8\pi n_p T_{\parallel,p}/B_0^2$, where n_p and B_0 are the proton density and background magnetic field, respectively. Temperature anisotropy contributes to the generation of EMIC waves (Conwall et al., 1970), and the proton distributions are modified to a linear marginally stable state (i.e., relaxed state), by EMIC wave-particle interaction. Plasma kinetic theory has shown the threshold conditions of ion cyclotron anisotropy instability as the upper bound on the relaxed proton distribution (Gary & Lee, 1994, Blum et al., 2009). Several satellite-based studies have suggested that this inverse relationship of EMIC waves can help determine their generation conditions and used as a proxy for their existence (Blum et al., 2009; Lin et al, 2014; Noh et al., 2018; Yue et al., 2019). However, the parameters a and b have not yet been clearly established.

Over several decades, numerous studies have examined the spatial distribution of EMIC waves in the magnetosphere using in-situ satellite observations (e.g., Allen et al., 2015, 2016; Anderson et al., 1992a, 1992b; Halford et al., 2010; Jun et al., 2019a, 2019b, 2021; Keika et al.,

2013; Kim et al., 2016b; Usanova et al., 2012; Matsuda et al., 2018a; Min et al., 2012; Meredith et al., 2014; Nakamura et al., 2014; Park et al., 2016, 2017; Saikin et al., 2015; Vines et al., 2019; Yue et al., 2019; Wang et al., 2015, 2017). These studies also demonstrated the relationship between EMIC wave distributions and geomagnetic conditions. For example, Min et al. (2012) reported that H- and He-EMIC waves are mainly observed at 10-12 R_E in the morning sector and at 8-12 R_E in the afternoon sector, respectively, using Time History of Events and Macroscale Interactions during Substorms (THEMIS) observations. Park et al. (2017) investigated the relationship between the occurrence of EMIC waves and the interplanetary magnetic field (IMF) using THEMIS observations and reported that H-EMIC waves have a peak occurrence region in the dawn sector during the northward IMF Bz. EMIC waves become more frequent beyond the geosynchronous orbit with an increase in the solar wind dynamic pressure on the dayside of the magnetosphere (e.g., Usanova et al., 2012; Park et al., 2016). Using the Van Allen Probes observations, Jun et al. (2019a, 2019b) reported that enhanced He-EMIC waves have the highest occurrence rate in the afternoon sector inside the plasmasphere associated with energetic particle injections. A recent study using Arase and Van Allen Probe observations (Jun et al., 2021) reported that H-EMIC waves in the morning sector at L > 8 are predominant during quiet geomagnetic conditions, while He-EMIC waves peak at L ~ 6-8 in the afternoon-dusk sector with strongly enhanced wave power during the storm main phase.

Magnetospheric convection during active geomagnetic conditions transports energetic protons in the energy range of 1-100 keV from the plasma sheet to the inner magnetosphere (e.g., Ebihara and Miyoshi, 2011; Yue et al., 2017a, 2017b). Convective transportation causes temperature anisotropy, which is the free energy source for exciting EMIC waves in the afternoon sector near the plasmapause (e.g., Jun et al., 2019a; Saikin et al., 2016; Yue et al., 2019, 2020; Wang et al., 2016). Saikin et al. (2016) performed a statistical study using the Van Allen Probes and reported that an increase in the occurrence of EMIC waves tends to move from noon to the afternoon sector at L~4-6 as the AE index increases. Based on the Van Allen Probes and GOES observations, Jun et al. (2019a) reported that He-EMIC waves are mainly found in the noon-afternoon sector inside the plasmasphere associated with substorm injections.

Recently, Jun et al. (2021) reported that H-EMIC waves outside the plasmasphere in the morning sector exhibit frequencies very close to f_{cH}. The unusual high-frequency EMIC waves exhibited a narrow bandwidth and were mainly detected on the dayside of the magnetosphere outside the plasmasphere under quiet geomagnetic conditions, indicating that energetic protons alone are not sufficient for exciting EMIC waves under these conditions. Studies have suggested that warm protons with energies of < 1 keV can possibly be a free energy source for generating unusual high-frequency EMIC waves in the morning sector (Teng et al., 2019; Min et al., 2021). Asamura et al. (2021) used Arase satellite observations to demonstrate that equatorial noise can lead to the resonant heating of suprathermal protons (10-100 eV), which can subsequently generate EMIC waves near f_{cH}.

Enhanced solar wind dynamic pressure can cause proton temperature anisotropy on the dayside of the magnetosphere. (Anderson and Hamilton, 1993; McCollough et al., 2010; Yue et al., 2009, 2010, 2011). Previous studies have investigated the relationship between increasing solar wind dynamic pressure and the occurrence of EMIC waves, suggesting that this process mainly drives EMIC waves on the dayside magnetosphere (Engebretson et al., 2002; Usanova et al., 2008, 2012; Nakamura et al., 2014; Park et al., 2016; Tsurutani et al., 2016; Jun et al., 2019b).

Recent studies proposed that EMIC waves can be excited in off-equatorial source regions

147 at high latitudes. When the magnetosphere is compressed, the temperature anisotropy increases
148 owing to drift-shell splitting and executing Shabansky orbits in the off-equatorial source regions
149 at higher L-shells, exciting EMIC waves within those regions (Allen et al., 2015, 2016;
150 McCollough et al., 2012; Vines et al., 2019).

151   Non-linear effects and mode conversion of EMIC waves can be possible candidate for
152 generating EMIC waves in the magnetosphere. Recently, it has been suggested that non-linear
153 interactions between energetic particles and EMIC waves can create a proton hill and hole in the
154 phase space, triggering rising and falling tone EMIC emissions, respectively (Sakaguchi et al.,
155 2013; Nakamura et al., 2016; Shoji et al., 2018, 2021). Miyoshi et al. (2019) reported that
156 plasmaspheric EMIC waves could also be generated through mode conversion from equatorial
157 noise.

158   Recent studies (Jun et al., 2019a, 2019b, 2021) have reported EMIC waves peak at different
159 regions in the inner magnetosphere, implying that they are generated by different processes
160 depending on the plasma environment. To understand their coupling, we performed a statistical
161 study of the energetic proton distributions associated with EMIC waves. In this paper, we present
162 the spatial distributions of EMIC waves as observed by the Arase satellites during 2017-2020 and
163 compare them with the associated proton distributions. We also computed the minimum resonance
164 energy of protons using the observed EMIC wave frequency and compared it to in-situ particle
165 observations.

166
167

2 Observation

2.1 Instruments

170   The Arase satellite, which belongs to the Exploration of energization and Radiation in
171 Geospace (ERG) project, was launched in December 2016. This satellite has an elliptical orbit with
172 a perigee and an apogee of 400 km and 6 R_E, respectively (Miyoshi et al., 2018a). The orbital and
173 spin periods are ~9.5 h and 8 s, respectively. The orbital inclination angle is 31˚. We used a
174 Magnetic Field Experiment (MGF; Matsuoka et al., 2018a) to identify EMIC waves. The partial
175 thermal pressure and pitch angle distribution for protons were obtained by a Low-Energy Particle
176 Experiments–Ion mass Analyzer (LEPi; Asamura et al, 2018) and a Medium-Energy Particle
177 Experiments-Ion Mass Analyzer (MEPi; Yokota et al., 2018). A High-Frequency Analyzer (HFA;
178 Kumamoto et al., 2018), part of the Plasma Wave Experiment (PWE) (Kasahara et al., 2018a),
179 provided the background electron density (N_e) derived from the observed upper hybrid resonance
180 (UHR) frequency. Satellite positions, such as the magnetic local time (MLT) and magnetic latitude
181 (MLAT) in solar magnetic coordinates, were obtained from ERG Level-2 orbit data (Miyoshi et
182 al., 2018c). The L* values and estimated equatorial magnetic field intensity were obtained from
183 ERG Level-3 orbit data (Miyoshi et al., 2018d) based on the Tsyganenko-Sitnov 2005 (TS05)
184 magnetic field model (Tsyganenko and Sitnov, 2005).

185

2.2 Data Analysis

2.2.1 Spectral analysis of the magnetic field

We computed the dynamic spectra of the magnetic field to detect the EMIC waves in the frequency domain. The original Level-2 magnetic field data measured by the MGF instrument contained harmonic spin-tone noises, thus we applied the spin-tone reducing method of Imajo et al. (2021) to the 64 Hz magnetic field waveform dataset. To obtain clean wave signals, we subtracted the 10 s moving average magnetic field data from the original data. We then rotated the magnetic field vector into the mean-field-aligned (MFA) coordinate system (Takahashi et al., 1990) using a 32-s moving average. The x-, y-, and z-components in the MFA coordinate system are in the radial (outward), azimuthal (eastward), and parallel (northward) directions to the ambient magnetic field, respectively. Finally, using a 64-s time window (4,096 data points) and a 15-s moving window, we applied a fast Fourier transform to the rotated waveform dataset to obtain the spectral matrix of each component in time and frequency space. Thus, the frequency and time resolution of the spectral matrix were 0.0156 Hz and 15 s, respectively.

2.2.2 Energetic proton data analysis

LEPi and MEPi measured the differential flux of ions with energies of 30 eV/q - 25 keV/q and 9.6-187 keV/q, respectively. Their sampling time for three-dimensional distribution function was ~8 s. We used the nominal mode observation data from two instruments, and they retained information on the three-dimensional distribution of ion fluxes. Using three-dimensional distribution functions of protons and an 8 s spin-averaged magnetic field, we computed the pitch-angle distribution (PAD) of protons with 11.25° pitch-angle bins. All PAD data from LEPi and MEPi were averaged over a 1-min time window.

Before combining the PAD obtained from the two ion instruments, inter-calibration was performed to obtain continuous proton flux variations in the energy range of 30 eV/q to 187 keV/q. We computed the spin-averaged ratio between LEPi and MEPi for their overlapping energy range (8-25 keV/q), which was used inter-calibration. The ratio was averaged over a 1-day time window. Using the derived ratio, the flux of MEPi in the energy range of 25-187 keV/q was changed, while the instrument sensitivity was not necessarily constant over the entire energy range. The average and standard deviation of the ratio for the entire period (2017-2020) are 1.27 and 0.34, respectively. The combined energy range of 30 eV/q-187 keV/q for the protons was sufficient to investigate their distributions from warm plasma (> 30 eV) to ring current (~ several tens to a few hundred keV) populations (Daglis et al., 1999; Jahn et al., 2017).

The partial proton pressures in the directions perpendicular ($P_\perp$) and parallel ($P_\parallel$) to the ambient magnetic field were calculated using the energy (E) and pitch-angle (α) distributions of the differential energy flux ($J(E, \alpha)$). We used the inter-calibrated proton PAD data in the energy range of 30 eV/q-187 keV/q in the following equations (De Michelis et al., 1999; Imajo et al., 2019; Yue et al., 2018):

$P_\perp = \pi \sum_E \sum_\alpha \sqrt{2m_p E} J(E, \alpha) sin^3 \alpha \Delta E \Delta \alpha$

$P_\parallel = 2\pi \sum_E \sum_\alpha \sqrt{2m_p E} J(E, \alpha) cos^2 \alpha \sin \alpha \, \Delta E \Delta \alpha$ (2)

where m_p is the proton mass, ΔE is the energy channel width, and $\Delta \alpha$ is the pitch angle bin width (11.25°). We then computed the temperature anisotropy ($T_\perp / T_\parallel$) using the obtained partial proton pressure, except for the small $P_\parallel$ ($P_\parallel < 0.1 \, nPa$), because they became unreliable.

229 The parallel plasma beta ($\beta_\parallel$) is defined as the ratio between the parallel proton pressure
230 and local magnetic pressure, as follows:

231 $\beta_\parallel = 2\mu_0 P_\parallel / B_{local}^2$ (3)

232 where μ_0 is the permeability of free space.

233

2.2.3 Calculation of the minimum resonance energy for protons

235 We calculated the plasma dispersion relation for electromagnetic waves propagating in the
236 parallel direction with respect to the ambient magnetic field in a cold plasma containing a mixture
237 of proton, helium, and oxygen ions (Meredith et al., 2003; Stix 1962; Walker, 1993). The
238 dispersion relation for the L-mode is defined as

239 $\dfrac{c^2 k^2}{\varpi^2} = 1 - \dfrac{\varpi_{pe}^2}{\varpi(\varpi + |\Omega_e|)} - \sum_{l=1}^{3} \dfrac{\varpi_{pl}^2}{\varpi(\varpi - \Omega_l)}$ (4)

240 where ϖ is the angular frequency ($\varpi = 2\pi f$), ϖ_{pe} and ϖ_{pl} are the electron and proton plasma
241 frequencies, respectively. Ω_e is the electron cyclotron frequency, and Ω_l is the ion cyclotron
242 frequency of the l species. The suffix l denotes the ion species, with values $l = 1, 2$, and 3 referring
243 to the proton, helium, and oxygen ions, respectively.

244 It is important to consider the ion composition ratio (H^+:He^+:O^+) in the dispersion relation
245 of EMIC waves. The direct measurement of the ion composition ratio was not available because
246 the minimum energy of the LEPi instrument used in this study was 30 eV. Total ion composition
247 is highly dependent on the geomagnetic activity, particularly the geomagnetic storm phase. For
248 example, the O^+ composition increases the total ion composition owing to a large increase in hot
249 O^+ during the main phase of geomagnetic storms (e.g., Yue et al., 2018). However, it is not
250 necessary to consider the influence of hot heavy ion composition on EMIC wave growth at heavy
251 ions gyrofrequencies (Silin et al., 2011). Instead, we considered the validity of the cold ion
252 compositions to calculate a reliable dispersion relationship for EMIC waves from previous studies
253 (e.g., Omura et al., 2010; Pakhotin et al., 2013; Silin et al., 2011). Jun et al. (2021) has reported
254 that the regions of peak EMIC wave occurrence have different geomagnetic preferences for their
255 generations. H-EMIC waves are predominantly observed in the morning sector outside the
256 plasmasphere during quiet conditions, whereas He-EMIC waves tend to be observed in the
257 afternoon sector inside the plasmasphere during disturbed conditions (Jun et al., 2019a and 2021).
258 To calculate the proton minimum resonance energy, we considered two empirical nominal ion
259 compositions: H^+:He^+:O^+=0.85:0.1:0.05 under the general geomagnetic conditions for H-EMIC
260 waves (Meredith et al., 2003), and H^+:He^+:O^+=0.97:0.02:0.01 for He-EMIC waves inside the
261 plasmasphere (Silin et al., 2011).

262 For protons, the resonance condition with L-mode waves is

263 $\varpi - k_\parallel v_\parallel = \dfrac{\Omega_p}{\gamma}$ (5)

264 where $\gamma = (1 - v^2/c^2)^{-1/2}$ and $v^2 = v_\perp^2 + v_\parallel^2$. Using the value of k from Eq. (4) and Eq. (5) and
265 substituting $v_\perp = 0$, the minimum resonance energy for protons, $E_{p,min}$, is determined by the
266 following equation:

267 $E_{p,min} = (\gamma - 1)m_p c^2$.   (6)

268   $E_{p,min}$ was calculated using the equatorial magnetic field intensity obtained using the TS05 model
269   for the cyclotron frequency and local background electron density for the plasma frequency.

270

271   **2.3 Event selection**

272   We collected the EMIC wave events observed by the Arase satellite in 2017-2020 based
273   on the event selection method of Jun et al. (2019a). The selection criteria were as follows:

274   1. The spectral structures of EMIC waves must be observed below f_{cH} in the perpendicular
275   magnetic field component of the dynamic spectrum.

276   2. The wave power and minimum duration of EMIC waves must be $> 10^{-4}$ nT^2/Hz and 5
277   min, respectively.

278   3. The background and artificial noises that have lower degrees of polarization and
279   coherences (< 0.5) must be excluded from the event list.

280   4. If the harmonic-like events are observed simultaneously, only the fundamental wave
281   structures were considered as an individual event.

282   As O-EMIC waves are difficult to distinguish from other ultra-low frequency emissions
283   because of their extremely low frequency in the region beyond L*>4 in the magnetosphere, we
284   disregarded them in this study. Therefore, we only categorized the selected EMIC waves based on
285   the equatorial ion cyclotron frequencies, i.e., H- and He-EMIC waves.

286   To determine $E_{p,min}$ associated with the observed EMIC waves, we collected the
287   frequency of the peak wave power within the selected frequency boundary as the central frequency.
288   Based on the wave analysis of Jun et al. (2019b), we derived the central frequency and polarization
289   sense of the observed EMIC waves every 1 min during the wave event interval.

290   Figure 1 presents an EMIC wave event observed by the Arase satellite on January 4th 2019
291   at 1500-1620 UT: a background electron density derived from the UHR frequency (Figure 1a), the
292   dynamic spectrum of the perpendicular component of the magnetic field with the equatorial gyro
293   frequencies for H$^+$, He$^+$, and O$^+$ (Figure 1b), temperature anisotropy $T_\perp/T_\parallel$ (Figure 1c), parallel
294   plasma beta $\beta_\parallel$ (Figure 1d), and proton pitch-angle distributions at different energy ranges (Figure
295   1f-1k). EMIC waves were well-defined below f_{cHe}, as He-EMIC waves, at 1520-1600 UT (Figure
296   1b). The Arase satellite was located ~18 MLT at L~6 near the magnetic equator (MLAT~5˚), with
297   a background density of 80 cm^{-3} (Figure 1a). $T_\perp/T_\parallel$ suddenly dropped and quickly recovered to its
298   initial value immediately before onset of the EMIC wave (~1520 UT) (Figure 1c). Figure 1d shows
299   an increase in $\beta_\parallel$ just before the EMIC wave event, which remained roughly constant during the
300   event. The proton omniflux distributions revealed flux enhancement at energies from 100 keV/q
301   with the EMIC wave event, the lower boundary of which extended to several keV/q (Figure 1e).
302   Note that the $E_{p,min}$ at 1540-1545 UT was discontinuous as the central frequency was not selected
303   due to out of our event criteria between the two EMIC wave portions.

304
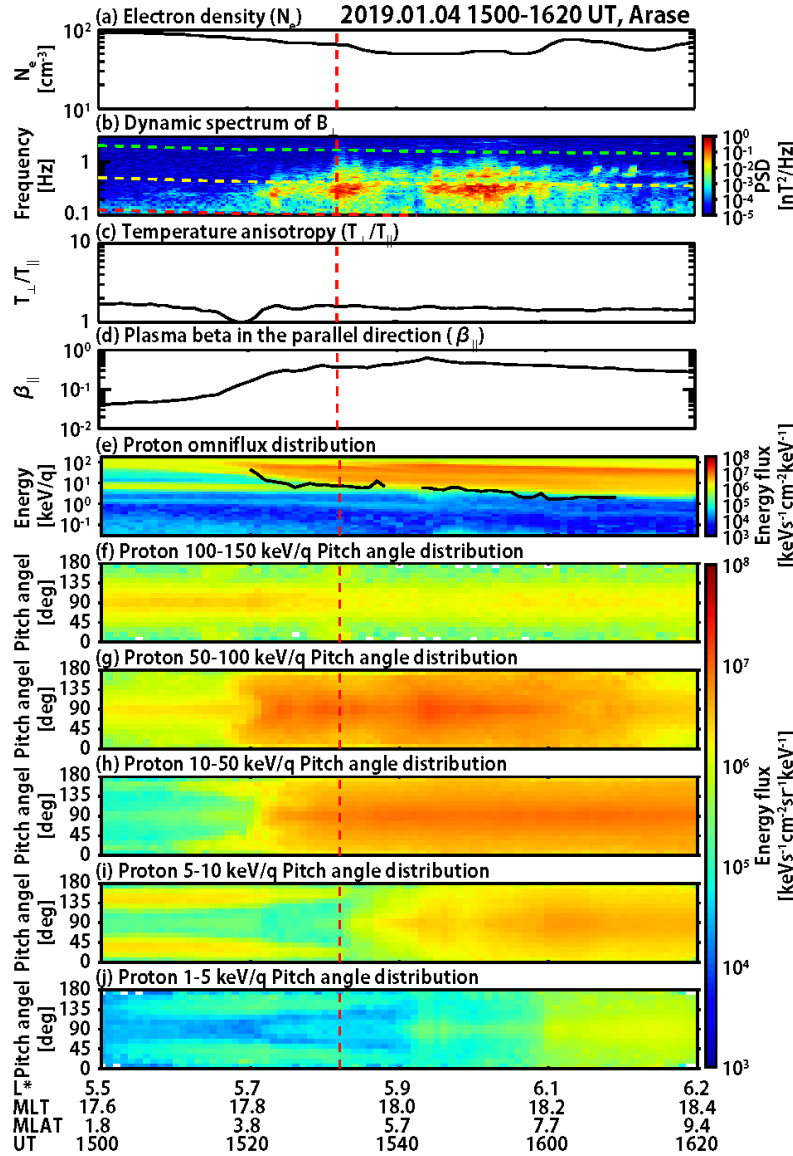
Figure 1. An EMIC wave event on January 4th, 2019 at 1500-1620 UT observed by the Arase satellite. (a) Background electron density (N_e), (b) perpendicular dynamic spectrum of the magnetic field ($B_\perp$) obtained by the MGF instrument, (c) temperature anisotropy ($T_\perp/T_\parallel$), (d) parallel plasma beta ($\beta_\parallel$), (e) energy spectrum of inter-calibrated proton omniflux distribution, and (f-k) pitch-angle distributions of energetic protons at energies of (f) 100-150, (g) 50-100, (h) 10-50, (i) 5-10, (j) 1-5 keV/q. The green, yellow, and red curves in Figure 1b represent the equatorial H$^+$, He$^+$, and O$^+$ gyrofrequencies, respectively. The red horizontal dashed line indicates 1532-1533 UT shown in Figure 2. The black solid curve in Figure 1e denotes the computed minimum proton resonance energy ($E_{p,min}$) using the central frequencies of observed He-EMIC waves.

314   We focused on the development of energetic proton distributions associated with EMIC
315   waves. The variation of $E_{p,min}$ gradually decreased from 44.2 to 1.8 keV (Figure 1e) and was well
316   consistent with the lower boundary of the H$^+$ flux enhancements. This indicates that the proton

317 flux enhancement in this energy range may be related to the major drivers of the observed EMIC
318 waves. Figures 1g-1j present the proton pitch angle distributions at different energy steps. Except
319 for the 100-150 keV/q range (Figure 1f), energy fluxes at energies of 1-100 keV/q (Figures 1g-1k)
320 generally exhibited sudden enhancement among all pitch angles during the EMIC wave event, and
321 the highest energy fluxes appeared at pitch angle of 90˚. Interestingly, Figures 1h-1j show that the
322 pitch angle structures seemed to be immediately shifted from field-aligned to pancake-like
323 distributions when $E_{p,min}$ reached the energy ranges of the lower boundary of the sudden flux
324 enhancement. This sudden change in energetic proton distributions depending on $E_{p,min}$ probably
325 occurred from the mixture of not only the energetic particle input driving EMIC waves, but also
326 the pancake distributions by EMIC pitch-angle scattering.

327   We described $E_{p,min}$ by solving the cold plasma dispersion relation based on the
328 parameters observed during wave activity. Figure 2 shows an example of the dispersion relation
329 (Figure 2a) and the corresponding $E_{p,min}$ (Figure 2b) at the time marked by the red dashed line in
330 Figure 1. The parameters used for these calculations are labeled in Figure 2. First, we obtained $k_{\parallel}$
331 from the dispersion relation (Figure 2a) using the central frequency with the peak wave power. We
332 then applied $v_{\parallel}$ obtained from Eq. (5) to finalize $E_{p,min}$ (Figure 2b). In Figure 2, the central
333 frequency was 0.3 Hz (a normalized frequency of 0.18 f_{cH}); thus the corresponding $E_{p,min}$ was
334 7.22 keV. $E_{p,min}$ was recorded every 1 min during the wave duration(black solid line in Figure
335 1e).
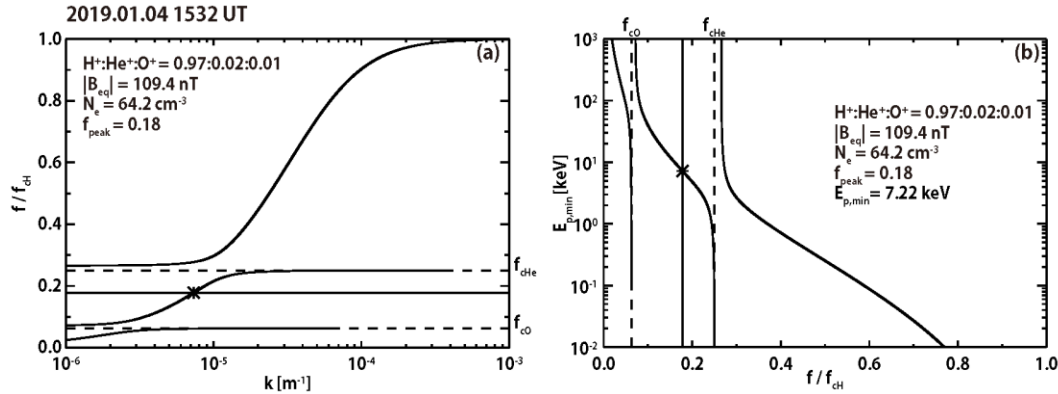
337 **Figure 2**. (a) Dispersion relation and (b) corresponding minimum resonance energy at
338 1532-1533 UT on January 4th, 2019. The parameters used for this calculation are indicated in the
339 figure.

3 Statistical Results

342   From the event selection, we identified 211.4 and 517.5 hrs of H- and He-EMIC waves,
343 respectively, observed by the Arase satellite from May 2017 to December 2020.

### 3.1 Spatial Distributions of EMIC waves and Electron Density

346   We identified EMIC waves for a 43-month period (May 2017-December 2020) using Arase
347   observations. Figure 3 presents the distributions of dwell times and EMIC wave occurrence rates
348   in the L*-MLT plane. The bin sizes for L*-MLT were 1 h in MLT with 0.5 in L* shell in the L*
349   range in 2-9. The dwell time of the Arase satellite was well distributed over all MLT and L* shells,
350   providing sufficient spatial coverage to investigate the statistical characteristics of EMIC waves in
351   the inner magnetosphere (Figure 3a). Occurrence rates of the EMIC waves were evaluated as the
352   total observed EMIC wave time divided by the dwell time in each bin (Figure 3b). We took into
353   account only the regions where the wave occurrence rate exceeded 1 % to focus on the major
354   EMIC wave generation regions. Two significant peak EMIC wave distributions were observed: 3-
355   8 MLT at L* = 7.5-9 and 11-20 MLT at L* = 5-9. These distributions were consistent with the
356   results of previous studies using in-situ satellite observations (e.g., Jun et al., 2021; Keika et al.,
357   2013; Min et al. 2012; Usanova et al., 2016).

358
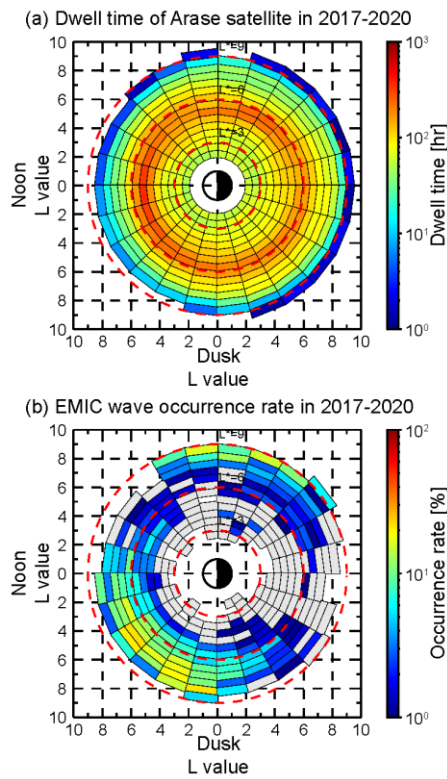
359   **Figure 3.** (a) Dwell time and (b) EMIC wave distribution in the L*-MLT plane observed by the
360   Arase satellite from May 2017 to December 2020. The gray regions indicate EMIC wave
361   occurrence rate < 1 %. The red circles denote L* = 3,6, and 9.

362

363   Figure 4 presents the MLAT distributions of dwell times and EMIC wave occurrence rates
364   for each 6-hour MLT bin. The bin sizes for Re-MLAT were 0.5 in Re with 5° in MLAT in the
365   MLAT range of |40|°. Even though the Arase satellite had limited observations in the Southern
366   Hemisphere at 09-15 MLT bin due to its orbit in 2017-2020, we had sufficient observational
367   coverage for this study (Figures 4a-4d). We found that EMIC waves were predominant at higher
368   MLAT (Figures 4e-4h). Typical EMIC waves were generated near the magnetic equator and

369   propagated to higher latitudes along the field line. Previous studies (Usanova et al., 2012; Min et
370   al., 2012) have reported higher EMIC wave occurrence rates in the outer magnetosphere.
371   Therefore, the appearance of peak EMIC wave occurrence at higher MLAT resulted from the
372   propagated waves at higher L* shells. It should be noted that the MLAT distributions of EMIC
373   waves with broad observational coverage in this study were facilitated by novel high-MLAT
374   measurements made by the Arase satellite.

375
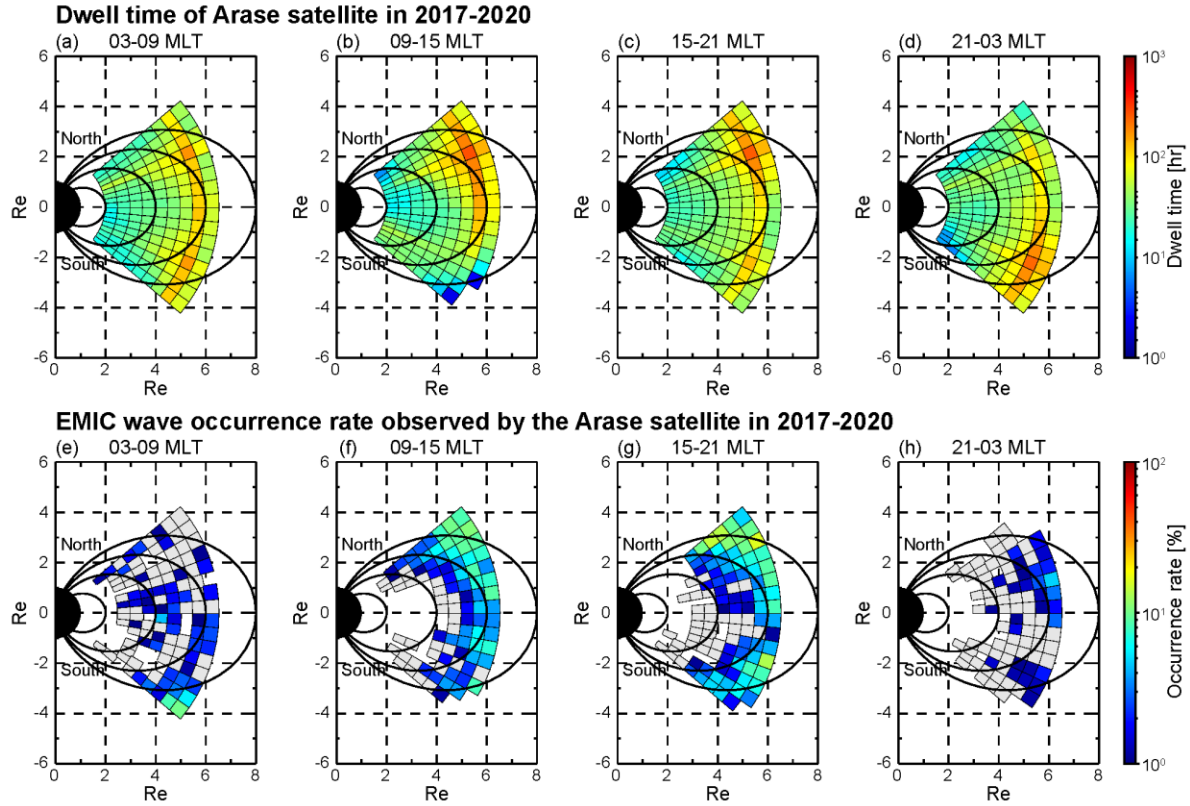
Figure 4. (a-d) Dwell time and (e-h) EMIC wave distribution at each 6-hour MLT sector in the
Re-MLAT plane observed by the Arase satellite from May 2017 to December 2020. The gray
regions indicate EMIC wave occurrence rate < 1 %. The black curves show the field lines at
L*=2,4,6, and 8.

380

381   In Figure 5, all EMIC wave events were divided into H- and He-EMIC waves according to
382   equatorial ion gyrofrequencies using the estimated equatorial magnetic field intensity from the
383   TS05 geomagnetic model. To investigate the dependence on background electron density, we
384   averaged the electron densities associated with EMIC waves in each bin.

385   Based on Figure 5, we identified three distinct wave occurrence regions with the wave
386   occurrence rate > 10 %, depending on the frequency band and N_e. In Figure 5a, H-EMIC waves
387   had two different peak occurrence regions in 3-8 MLT at L* = 7.5-9 (Peak Region 1; PR1) and in
388   12-15 MLT in L*=6.5-8 (Peak Region 2; PR2). Both regions exhibited lower N_e (< 10 cm^{-3}) as
389   seen in Figure 5c, indicating that the waves were observed outside the plasmasphere. However,
390   He-EMIC waves showed a broad occurrence region at 12-20 MLT at L* = 5.5-85 (Peak Region 3;

391 PR3) in Figure 5b. As N_e in the broad occurrence region gradually decreased from lower to higher
392 L* shells as shown in Figure 5d, it is difficult to simply identify whether wave activities occurred
393 inside or outside the plasmasphere. If we adopt a specific value of $N_e \sim 40 cm^{-3}$ (e.g., Goldstein et
394 al., 2014) as a proxy to roughly locate the plasmapause, we can assume that He-EMIC waves in
395 PR3 occurred either inside the plasmasphere, plasmaspheric plumes, or near the plasmapause. The
396 dawn-dusk asymmetry of the peak occurrence regions between H- and He-EMIC waves agreed
397 well with the EMIC wave distributions obtained by previous in-situ satellite observations (e.g.,
398 Min et al., 2012; Kim et al., 2016b; Jun et al., 2021).

399
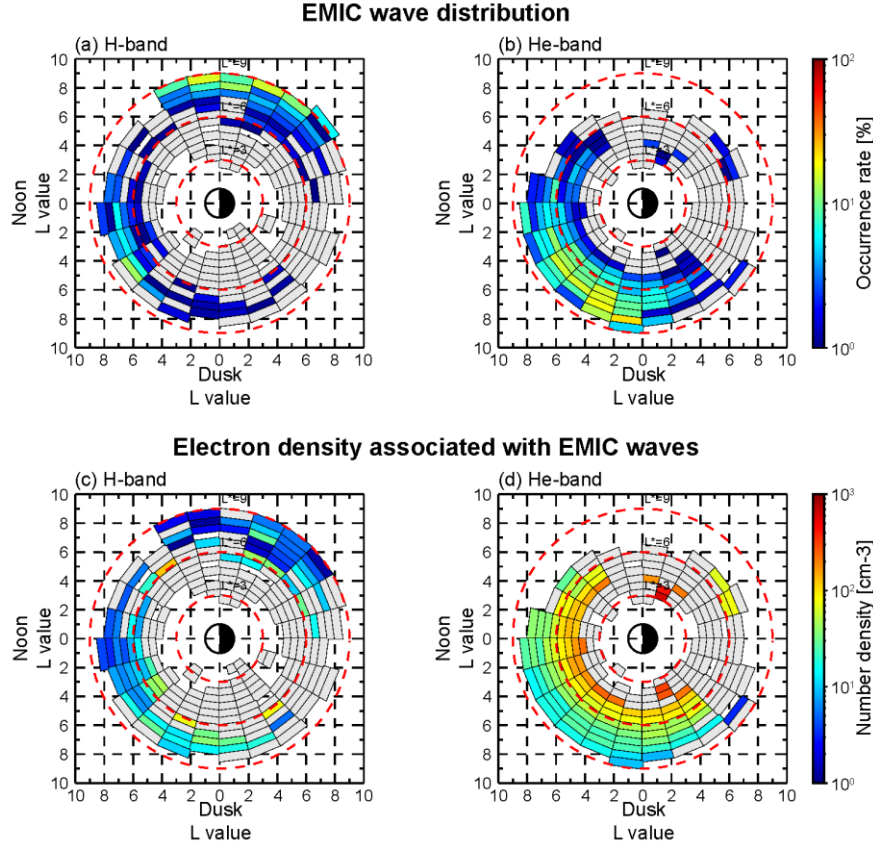
400 **Figure 5.** (a) H- and (b) He- EMIC occurrence rates, and related electron density distributions
401 for (c) H-band and (d) He-band.

402

403 **3.2 Temperature Anisotropy-Parallel Plasma Beta conditions with EMIC waves**

404 Even though the temperature anisotropy $T_\perp/T_\parallel$ and parallel plasma beta $\beta_\parallel$ varied with the
405 EMIC wave activity (Figure 1), it was not sufficient to demonstrate the relationship between these
406 parameters and EMIC wave activity from a single case study. Thus, we examined their inverse
407 relationship between $T_\perp/T_\parallel$ and $\beta_\parallel$ associated with EMIC waves through a statistical analysis
408 (Figure 6) showing the statistical results of EMIC wave distributions (Figures 6a-6b), |MLAT|
409 (Figures 6c-6d), and polarization sense (Figures 6e-6f) in $T_\perp/T_\parallel$- $\beta_\parallel$ diagrams for H- and He-EMIC
410 waves. The threshold of proton cyclotron instability is defined by Eq. (1) (Blum et al 2009; Denton

411 et al., 1994; Gary et al., 1994; Yue et al., 2019). We obtained a=1.3 and b=0.35 by the upper fitting
412 boundary of our observations, and the threshold lines were marked with the black dashed curves
413 in Figure 6.
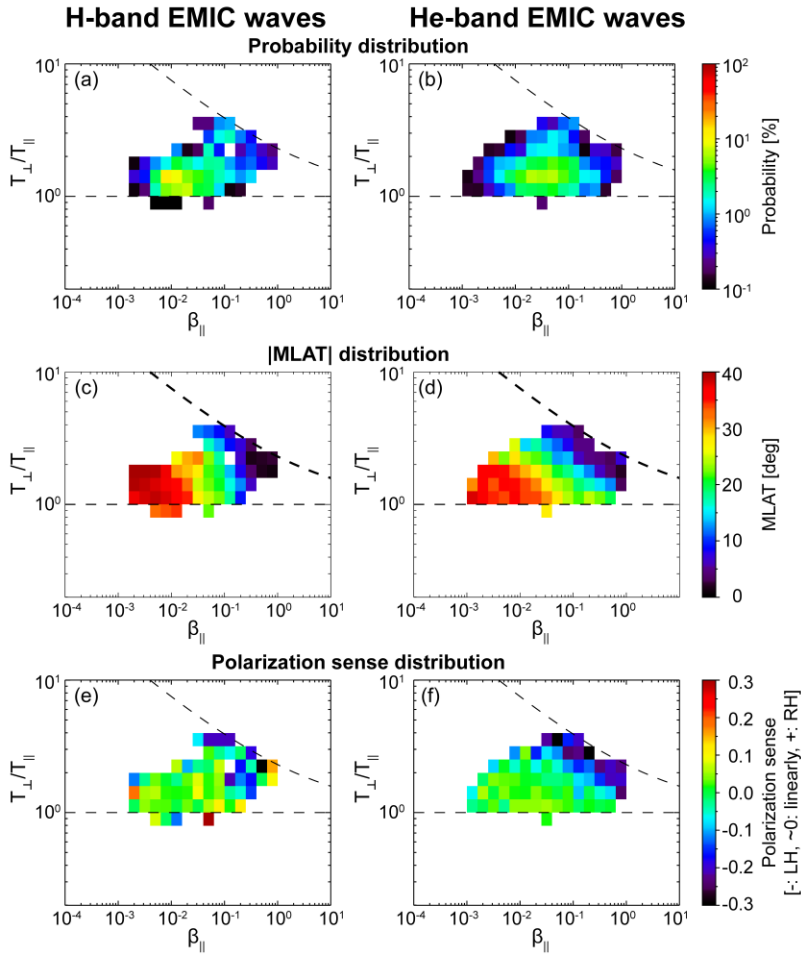
Figure 6. Distribution of (a-b) probability of EMIC waves, (c-d) average |MLAT|, (e-f)
polarization sense for H- and He-EMIC waves as a function of proton temperature anisotropy and
parallel plasma beta based on the Arase observations from May 2017 to December 2020. The
dashed curve on each panel is the threshold of proton cyclotron instability obtained from plasma
kinetic theory of $\frac{T_\perp}{T_\parallel} = 1 + \frac{a}{\beta_\parallel^b}$. We used a=1.3 and b= 0.35 obtained by the upper profile of EMIC
wave distributions.

Overall, EMIC waves exhibited significant tendencies in |MLAT| and polarization sense
depending on the plasma conditions regardless of the wavebands. The observed EMIC waves near
the threshold of the proton cyclotron instability had left-handed polarization close to the magnetic
equator ($< 5°$ |MLAT|), indicating that they were generated near the magnetic equator. As |MLAT|
increased, the polarization sense for He-EMIC waves clearly varied from left-handed to linear
polarization (Figures 6d and 6f), while the polarization sense for H-EMIC waves appeared roughly
constant with linearly polarization even near the magnetic equator (Figures 6c and 6e). The former

429   indicates polarization reversal during propagation from the wave source region to higher latitudes
430   due to the changing magnetic field intensity (Kim et al., 2016a). We also found that the latitude of
431   the changing polarization sense from left-handed to linear was ~ 20° MLAT (Figure 5g),
432   corresponding to the crossover latitudes of EMIC waves in previous studies (e.g., Loto'aniu et al.,
433   2005; Jun et al., 2019b; Yue et al., 2019). The latter is related to linearly polarized H-EMIC waves
434   by the solar wind dynamic pressure variations as reported by Jun et al. (2019b).

435

436   **3.3 Proton Distributions associated with EMIC waves**

437   To investigate the influence of EMIC waves on energetic proton distributions in each
438   region, the energetic proton PAD associated with EMIC waves (top panels) and the energy flux
439   ratio of the PAD between with and without EMIC waves (bottom panels) were presented (Figure
440   7). The PAD was binned with a bin size of 11.25° for the pitch angle and energy range from 30 eV
441   to 185 keV at each peak occurrence region. Figures 7a-7c show the average PAD associated with
442   EMIC waves in each peak occurrence region. Figures 7d-7f show the flux ratio between cases with
443   and without EMIC waves in each peak occurrence region. The reddish and bluish regions indicate
444   an increase and decrease in the proton flux associated with EMIC waves, respectively. We assumed
445   that an increase in proton flux with EMIC waves at all pitch angles at certain energies is strongly
446   related to not only energetic particle input as the free energy source of EMIC waves, but also the
447   deformation of pitch-angle scattering by EMIC wave-particle interaction (e.g., Sigsbee et al.,
448   2019).

449   Proton distributions associated with EMIC waves differed significantly depending on peak
450   occurrence regions (Figure 7), supporting that EMIC waves supports that EMIC waves have
451   different free energy sources depending on their geomagnetic environments (Jun et al., 2021).

452   For example, Figure 7a shows the weakest flux level among the three regions. Instead, PR1
453   shows a clear flux enhancement in the warm plasma energy range (E < 10 keV/q) over the entire
454   pitch-angle range compared to the other regions (Figures 7a nad 7d). This is related to the supply
455   of warm protons (E < 10 keV) due to $\mathbf{E} \times \mathbf{B}$ drift by the combination of the electric and magnetic
456   fields (Yue et al., 2018). For PR2 (Figures 7b and 7e), we observed two types of flux enhancements
457   associated with EMIC waves. One appeared at energies of 1-100 keV/q in field-aligned directions,
458   and the other was among all pitch-angles over a limited energy range of 2-8 keV/q. Figure 7c for
459   PR3 that shows the highest flux level appeared at energies of 1-100 keV/q among all the peak
460   occurrence regions. We also found a significant increase in the proton energy flux > 2 keV/q at all
461   pitch-angles for PR3 (Figure 7f). This hot proton population is transported from the plasma sheet
462   in the magnetotail to the dusk sector during the substorm intervals, and contributes to drive the
463   temperature anisotropy, causing enhanced EMIC waves in the afternoon sector (e.g., Saikin et al.,
464   2016; Jun et al., 2019a and 2021). PR3 showed the another flux enhancement in the warm plasma
465   region (E < 100 eV) which might be due to another processes such as EMIC wave heating by non-
466   linear wave-particle interactions (Ma et al., 2019; Shoji et al.,2021).

467
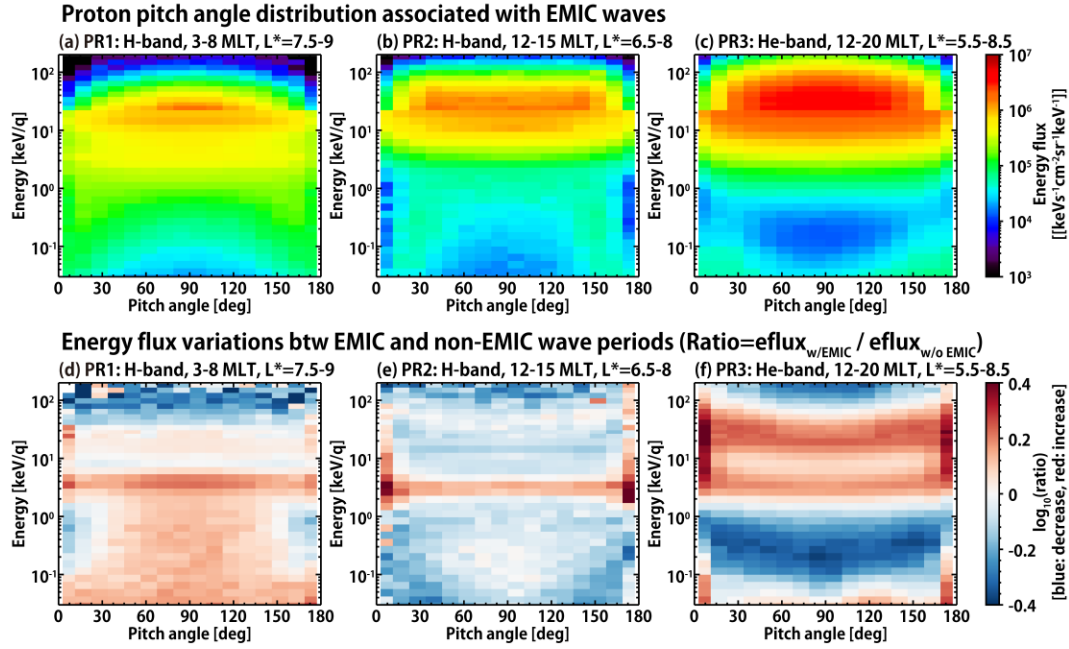
Figure 7. (a-c) Proton pitch-angle distribution associated with EMIC waves as a function of energy and pitch angle at each peak occurrence region. (d-f) Energy flux ratio between with and without EMIC waves at each peak occurrence region.

471

3.4 The Relationship Between EMIC Wave Frequency and Minimum Resonance Energy

Figure 8 shows the normalized distributions of $E_{p,min}$ as a function of the frequency normalized by f_{cH} in each peak occurrence region. We took the central frequency that satisfied our event selection criteria for the calculation of $E_{p,min}$ during the EMIC wave periods. The vertical dashed lines denote ion gyrofrequencies (f_{cH}, f_{cHe}, and f_{cO}). The bin sizes of the normalized frequency and $E_{p,min}$ were 0.01 on a linear scale and 0.05 on a logarithmic scale, respectively. We adopted two ion compositions for two different wavebands: $H^+:He^+:O^+=0.85:0.1:0.05$ for H-EMIC waves (PR1 and PR2), and $H^+:He^+:O^+=0.97:0.02:0.01$ for He-EMIC waves (PR3) (Section 2.4). The vertical closed arrow bars in each panel indicate the observed energy ranges, showing an increase in proton fluxes obtained from Figure 7d-7f. We divided the total number of data points in each peak occurrence region to obtain the normalized distributions.

Overall, the $E_{p,min}$ distributions in all regions were in good agreement with the energy range where the flux enhancements were associated with the EMIC waves (Figures 7d-7f). We also found distinct distributions at each peak occurrence region. Even though PR1 and PR2 took into account same waveband (H-EMIC waves), the $E_{p,min}$ distributions were completely different. Because the normalized frequency for PR1 was widely distributed from 0.3 to 0.9, $E_{p,min}$ varied from 1 eV to 100 keV with a uniform distribution (Figure 8a). $E_{p,min}$ was locally distributed from 1 keV to 1 MeV, with limited normalized frequencies of 0.3-0.5 (Figure 8b). For PR3 (Figure 8c), the observed energy ranges with flux enhancements were consistent with the peak $E_{p,min}$

492 distributions located at 2-100 keV, except for the region at energies of < 100 eV.

493
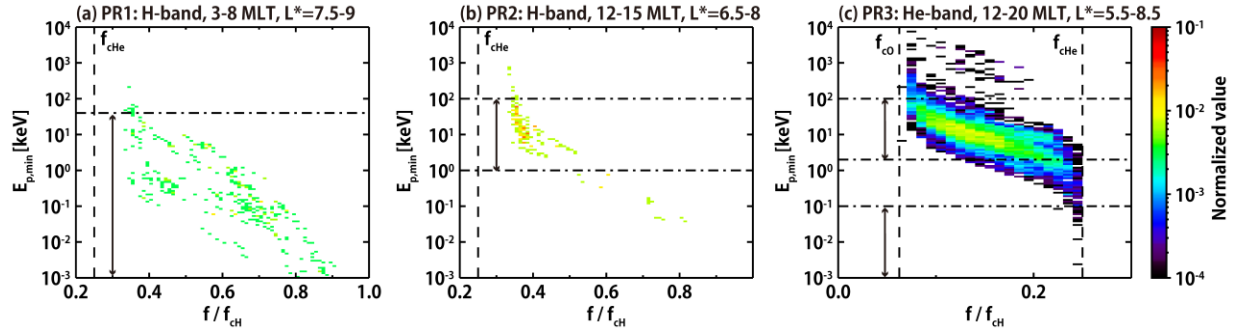
Figure 8. Normalized distribution as a function of the proton minimum resonance energy
($E_{p,min}$) and normalized frequency by f_{cH} for each peak occurrence region. Vertical dashed lines
represent the equatorial ion gyrofrequencies. Horizontal dashed lines denote the observed flux
enhancement energy range obtained from Figure 7.

498

4 Discussion

In this study, we investigated the spatial distributions of EMIC waves and their associated
energetic proton distributions in the inner magnetosphere using the Arase satellite data from May
2017 to December 2020. We found three distinct peak occurrence regions of EMIC waves
depending on the waveband and the related background electron density. The observational and
theoretical characteristics of EMIC waves within each peak occurrence region are summarized in
Table 1.

	Peak Region 1 (PR1)	Peak Region 2 (PR2)	Peak Region 3 (PR3)
Peak occurrence regions	03-08 MLT, L* = 7.5-9	12-15 MLT, L* = 6.5-8	12-20 MLT, L* = 5.5-7.5
Waveband	H-band	H-band	He-band
Electron density	$N_e < 10$ cm^{-3} (outside the plasmasphere)	$N_e \sim 10\text{-}20$ cm^{-3} (outside the plasmasphere)	$N_e \sim 50\text{-}100$ cm^{-3} (inside or near the plasmasphere)
Proton distributions associated	Weakest flux level among all regions.	Similar distributions with PR1.	Strongest ring current population at E = 1-187 keV

with EMIC waves	Flux enhancements: - E < 40 keV/q (warm proton populations)	Flux enhancements: -E = 1-100 keV/q (field-aligned directions) -E = 2-4 keV/q (all pitch-angles)	Flux enhancements: -E = 2-187 keV/q -E < 100 eV/q (field-aligned directions)
The computed minimum resonance energy $(\boldsymbol{E_{p,min}})$	1 eV - 100 keV	1 keV - 1 MeV (some portions at ~0.1 keV)	0.1 keV - 1 MeV

506 **Table 1**. Summary of the characteristics of EMIC waves at four distinct peak occurrence regions
507 observed by the Arase satellite.

508

4. 1. The relationship between plasma kinetic theory and EMIC waves

510 We examined the inverse relationship between $T_{\perp,p}/T_{\parallel,p}$ and $\beta_{\parallel,p}$ associated with EMIC
511 waves as shown in Figure 6. EMIC waves were observed only in the anisotropy range between the
512 threshold of the proton cyclotron instability and $T_{\perp,p}/T_{\parallel,p} > 1$. In particular, the highest probability
513 of EMIC waves with left-handed polarization at the magnetic equator was near the threshold of
514 the proton cyclotron instability. After EMIC wave generation within the source regions, they
515 propagate approximately along the field lines to higher magnetic latitudes and experience a change
516 in the dispersion relation (Matsuda et al., 2021). We found that the polarization sense varied from
517 left-handed to linear as |MLAT| increased, indicating mode coupling and conversion during the
518 propagation of EMIC waves. Because the polarization sense changed to linear at |MLAT| ~ 20° on
519 average, this result was consistent with previous statistical studies of the EMIC wave source
520 boundaries on MLAT (e.g., Loto'aniu et al., 2005; Jun et al., 2019b; Yue et al., 2019). The
521 probability distribution of EMIC waves in $T_{\perp,p}/T_{\parallel,p}$-$\beta_{\parallel,p}$ diagram shifted away from the threshold
522 of proton cyclotron instability to a lower $\beta_{\parallel,p}$ with a constant $T_{\perp,p}/T_{\parallel,p}$ with an increase in |MLAT|.
523 This result can be explained by the average meridional distribution of hot (10-180 keV) protons as
524 shown by the Arase satellite (Imajo et al., 2019). Pressure anisotropy is roughly constant with
525 increasing MLAT, whereas $\beta_{\parallel,p}$ decreases as MLAT increases.

526 If $T_{\perp,p}/T_{\parallel,p}$ is independent and roughly constant on |MLAT|, we can assume an equatorial
527 parallel plasma beta using the estimated magnetic field intensity at the magnetic equator obtained
528 by the TS05 model. Figure 9 shows the probability distributions of EMIC waves in $T_{\perp,p}/T_{\parallel,p}$-$\beta_{\parallel,p}$
529 diagram within each peak region. The upper and lower panels use the local and equatorial magnetic
530 field intensities, respectively. Although we cannot estimate the appropriate $P_{\parallel,p}$ at the magnetic

531 equator, the highest probability of EMIC waves obtained from the equatorial parallel plasma beta
532 shifted near the threshold of ion cyclotron instability, except for PR2 (Figures 9d-9f).

533   If the threshold of ion cyclotron instability and the equatorial plasma parameters are well-
534 determined from observational and theoretical methods, we suggest that the inverse relationship
535 between $T_{\perp,p}/T_{\parallel,p}$ and $\beta_{\parallel,p}$ can be used as a proxy for the generation conditions of EMIC waves
536 using local plasma conditions. When the plasma condition is unstable for proton cyclotron
537 instability due to sufficient temperature anisotropy, EMIC waves are generated. During this
538 process, plasma distribution undergoes diffusion in the velocity space by EMIC wave-particle
539 interaction, leading to isotropic distributions by the ion cyclotron instability to a linear marginally
540 stable state (Denton et al., 2019; Yue et al., 2019). Unfortunately, this approximation for PR2 did
541 not reach the threshold for proton cyclotron instability. Thus, we could not demonstrate a clear
542 interpretation at this point, but we proposed that a non-linear process driven through the formation
543 of proton-hill/hole (Shoji et al, 2018, 2021) might put the distribution far from the stable state.
544 Nakamura et al. (2016) reported that EMIC rising/falling tone emissions caused by a proton-
545 hill/hole distributions were dominantly observed on the dayside at higher magnetic latitudes,
546 consisting of PR2. Future research target should investigate the influence of non-linear effects on
547 EMIC waves.
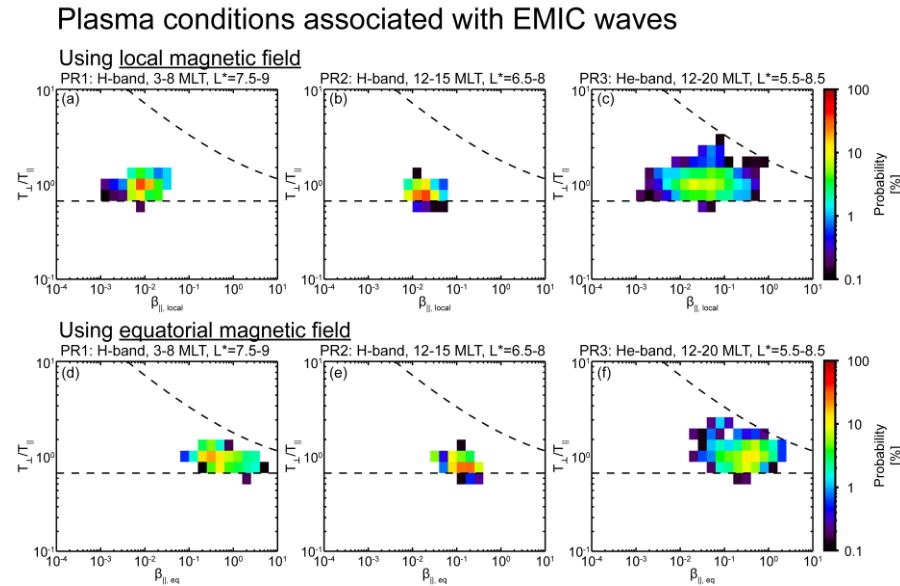
549 **Figure 9.** Probability distribution of EMIC waves for each peak occurrence region as a function
550 of proton temperature anisotropy and parallel plasma beta using (a-d) local magnetic field and (e-
551 h) the estimated equatorial magnetic field computed by a TS05 model. The dashed curves on each
552 panel are the thresholds of proton cyclotron instability as same as Figure 6.

553

554   4. 2. Possible generation processes and free energy sources of EMIC waves under different
555 geomagnetic environments

556   In this study, we found that EMIC waves at PR1 occurred in the morning sector at higher

557   L-shells (L* = 7.5-9) with broadly scattered normalized frequencies of 0.3-0.9. In Figure 7a, the
558   proton distributions associated with EMIC waves at PR1 exhibited the abundant warm proton
559   distributions with weaker ring current populations. The unusual high-frequency EMIC waves near
560   f_{cH} were predominantly observed within this region, and the computed $E_{p,min}$ was distributed
561   broadly from 40 keV to even a few eV. PR1 appeared to have different environments for the
562   generation of EMIC waves compared to those for typical EMIC waves, indicating that the ring
563   current populations having from a few tens to several hundreds of keV, known as typical free
564   energy sources of EMIC waves, are not always sufficient to be the major contributor on the wave
565   generation in the morning sector at higher L shells.

566   To understand the generation processes of EMIC waves at PR1, we proposed two
567   possibilities: broad source regions and a wide energy range of the free energy sources. If the initial
568   frequencies of EMIC waves are defined by the magnetic field intensity at their source regions, we
569   can assume broader distributions of the normalized frequencies as a result of the radially extended
570   source regions. However, the first assumption did not coincide with our observations (Figure 5a).
571   In contrast, for PR1, flux enhancements associated with EMIC waves appeared with wide energy
572   ranges of < 10 keV/q. Thus, the second possibility was deemed more reliable for EMIC waves at
573   PR1. Previous studies have proposed that the warm plasma cloak (E < 1 keV) with temperature
574   anisotropy in the morning sector can be a potential to drive temperature anisotropy for the EMIC
575   wave generation (Keika et al., 2013; Kim et al., 2016b). The low-energy protons (E < 10 keV) drift
576   to the east (dawn) due to convection and corotation drift motion, while the westward (toward dusk)
577   gradient and curvature drift motions dominate for energetic protons in the energy range of > 10
578   keV (Yue et al., 2017a, 2017b, and 2018). Using the Van Allen Probes and Arase observations,
579   Jun et al. (2021) reported that morning-side EMIC waves in the H-band were mainly observed
580   under quiet geomagnetic conditions. According to the relationship between the orientation of
581   interplanetary magnetic field (IMF) Bz and EMIC wave distributions (Park et al., 2017), H-EMIC
582   waves have peak occurrence regions in the dawn sector under northward IMF Bz conditions. They
583   suggested that $T_{\perp,p}/T_{\parallel,p}$ in the dawn sector increases due to the dominant effects of E × B drift
584   motion at energies of 1-25 keV during the northward IMF Bz intervals, causing H-EMIC waves
585   in that region.

586   Moreover, Teng et al. (2019) reported unusual EMIC waves near the proton gyrofrequency
587   associated with enhanced suprathermal protons (10-100 eV). These waves exhibited a very narrow
588   bandwidth and tended to be observed simultaneously with the magnetosonic waves. They also
589   reported that these waves were usually observed in the morning to noon sector based on the Van
590   Allen Probes observations. Asamura et al. (2021) used the Arase observations and identified that
591   magnetosonic waves cause resonant heating of suprathermal protons, which have temperature
592   anisotropy and drive high-frequency EMIC waves in the noon sector. Therefore, we suggest that
593   low-energy proton distribution, such as warm plasma (E < 1 keV), can be a possible candidate as
594   a free energy source for unusual high-frequency H-EMIC waves in the morning sector at higher
595   L-shells during quiet geomagnetic conditions.

596   We also found the other peak occurrence regions for H-EMIC waves in the noon sector at
597   L* = 6.5-8 (PR2). We could not find a significant coupling of EMIC waves with energetic proton
598   distributions for PR2 in this study. However, the peak EMIC wave occurrence region for R2 was
599   consistent with previous studies of H-EMIC driven in the lower density regions on the dayside by
600   the solar wind dynamic pressure (e.g., Jun et al., 2019a and 2021; Saikin et al., 2013; Park et al.,

2016; Usanova et al., 2012). When the ambient magnetic field is compressed by strong solar wind dynamic pressure, adiabatic heating occurs on the dayside magnetosphere, contributing to the enhancement of temperature anisotropy (Zhou and Tsurutani, 1999). During this process, the temperature anisotropy of energetic protons increases in all energy ranges, exciting EMIC waves on the dayside (Anderson and Hamilton, 1993).

We found a wide spatial distribution of He-EMIC waves from noon to the afternoon sector at L* = 5.5-8.5 with higher background electron densities (PR3). For the He-EMIC waves, the energy range of the obtained $E_{p,min}$ and their associated flux enhancements were in good agreement at 1-180 keV (Figures 7f and 8c). In particular, we found a clear ring current population in the proton PAD and the significant proton flux enhancement occurred in the energy range of 2-100 keV. Based on the Van Allen Probes observations, Jun et al. (2019a) reported that He-EMIC waves associated with particle injections generally occurred inside the plasmasphere in the afternoon sector. Yue et al. (2019) also reported that enhanced He-EMIC waves inside the plasmasphere were predominantly observed near the threshold of the proton cyclotron instability during strong AE intervals. From the current and previous studies, we suggest that the free energy source of EMIC waves for PR3 is the energetic particles transported from the plasma sheet into the inner magnetosphere during disturbed geomagnetic conditions. Hot anisotropic ions in the ring current population play an important role in driving the growth rate of EMIC waves, and the maximum wave growth rate was observed at lower frequencies as He-EMIC waves by the large plasma density (e.g., Cornwall et al., 1970; Lee et al., 2017; Chen et al., 2010). These He-EMIC waves in the afternoon sector are quite effective at resonating with the ring current populations in the cold plasma dominant regions (Jordanova et al., 2008). They also diffuse the hot protons from 90˚ to 0˚ and 180˚ pitch angles, causing the IPAs due to precipitating energetic protons (Sakagushi et al., 2007; Ozaki et al., 2016, 2020) and relativistic electrons (Miyoshi et al., 2008). Unfortunately, we could not interpret the clear reason for the flux enhancements associated with He-EMIC waves at energies < 0.1 keV for PR3 (Figure 7f). We infer a candidate that this might be related to ion heating at lower energies by EMIC wave-particle interactions and magnetosonic waves (Ma et al., 2019; Shoji et al., 2021).

PR3 showed a broad spatial distribution radially with relatively lower densities (Ne~ a few tens cm^{-3}) in the dusk sector at L* = 7-9 at higher |MLAT| (Figures 4 and 5). This region might have different plasma conditions for the generation of EMIC waves compared to those near the plasmapause, therefore we could not exclude other possibilities, such as off-equatorial generation process as a possible cause of EMIC waves in the dusk sector at higher L-shell regions (e.g., Allen et al., 2015, 2016; Vines et al., 2019). Based on the Arase and the Van Allen Probe observations (Jun et al., 2021), He-EMIC waves outside the plasmasphere were predominantly observed in the dusk sector at higher L-shell regions under moderate geomagnetic conditions. We could not determine whether the observed EMIC waves were freshly generated close to the off-equatorial source regions at higher magnetic latitudes or if they just propagated from the magnetic equator. Such a study can be conducted by examining the Poynting flux of EMIC waves using the magnetic and electric field instruments onboard the Arase satellite, which can be a future approach.

5 Conclusions

In this study, we investigated the spatial distributions of EMIC waves and the energetic

proton distributions associated with them in the inner magnetosphere using the Arase satellite data from May 2017 to December 2020. We found that EMIC waves were generated near the threshold of the proton cyclotron instability at the magnetic equator with a left-handed polarization sense, and propagated to a higher MLAT along the field line. During propagation, EMIC waves suffered polarization reversal at |MLAT|~20˚ from left-handed to linear. If it is possible to estimate the plasma conditions derived by $T_{\perp,p}/T_{\parallel,p}$ and $\beta_{\parallel,p}$ near the magnetic equator and determine an appropriate threshold for the proton cyclotron instability, we can predict the existence of EMIC waves by in-situ observations. We also found three peak occurrence regions of EMIC waves with different characteristics depending on the wavebands and ambient electron densities. We suggest that free energy sources of EMIC waves in different geomagnetic environments drive various types of EMIC waves, and they interact with energetic protons at different energy ranges. We will extend our future research to investigate the resonant conditions of relativistic electrons for different types of EMIC waves using in-situ satellite observations.

References

Allen, R. C. et al. (2015), A statistical study of EMIC waves observed by Cluster: 1. Wave properties. *Journal of Geophysical Research: Space Physics*, 120, 5574-5592. doi:10.1002/2015JA021333

Allen, R. C. et al. (2016), A statistical study of EMIC waves observed by Cluster: 2. Associated plasma conditions. *Journal of Geophysical Research: Space Physics*, 121, 6458-6479. doi:10.1002/2016JA022541

Anderson, B. J., Erlandson, R. E., & Zanetti, L. J. (1992a), A statistical study of Pc1-2 magnetic pulsations in the equatorial magnetosphere: 1. Equatorial occurrence distributions. *Journal of Geophysical Research*, 97(A3), 3075-3088, doi:10.1029/91JA02706

Anderson, B. J., Erlandson, R. E., & Zanetti, L. J. (1992b), A statistical study of Pc1-2 magnetic pulsations in the equatorial magnetosphere: 2. Wave Properties. *Journal of Geophysical Research*, 97(A3), 3089-3101. doi:10.1029/91JA02706

Anderson, B. J., & Hamilton, D. C. (1993), Electromagnetic ion cyclotron waves stimulated by modest magnetospheric compressions. *Journal of Geophysical Research*, 98, 11,369-11,382. doi:10.1029/93JA00605

Asamura, K., Kazama, Y., Yokota, S. et al. (2018), Low-energy particle experiments–ion mass analyzer (LEPi) onboard the ERG (Arase) satellite. *Earth Planets Space*, 70, 70. doi:10.1186/s40623-018-0846-0

Asamura, K., Shoji, M., Miyoshi, Y., Kasahara, Y., Kasaba, Y, et al. (2021), Cross-Energy Couplings from Magnetosonic Waves to Electromagnetic Ion Cyclotron Waves through Cold Ion Heating inside the Plasmasphere. *Physics Review Letter*, 127 (24), 245101(7). doi:10.1103/PhysRevLett.127.245101

Blum, L. W., MacDonald, E. A., Gary, S. P., Thomsen, M. F., & Spence, H. E. (2009), Ion observations from geosynchronous orbit as a proxy for ion cyclotron wave growth during storm times. *Journal of Geophysical Research*, 114, A10214. doi:10.1029/2009JA014396

Borovsky, J. E., Valdivia, J.A (2018), The Earth's Magnetosphere: A Systems Science Overview and Assessment. *Surveys in Geophysics*, 39, 817-859. doi:10.1007/s10712-018-9487-x

Chen, L., Thorne, R. M., Jordanova, V. K., Wang, C.-P., Gkioulidou, M., Lyons, L., & Horne, R. B. (2010), Global simulation of EMIC wave excitation during the 21 April 2001 storm from coupled RCM-RAM-HOTRAY modeling. *Journal of Geophysical Research*, 115, A07209. doi:10.1029/2009JA015075.

Cornwall, J. M., Coroniti, F. V., & Thorne, R. M. (1970), Turbulent loss of ring current protons. *Journal of Geophysical Research*, 75, 4699–4709. doi:10.1029/JA075i025p04699

716 Daglis, I. A., Thorne, R. M., Baumjohann, W., & Orsini, S. (1999), The terrestrial ring current:
717 Origin, formation, and decay. *Reviews of Geophysics*, 37(4), 407–438.
718 doi:10.1029/1999RG900009
719
720 De Michelis, P., Daglis, I. A., & Consolini, G. (1999), An average image of proton plasma pressure
721 and of current systems in the equatorial plane derived from AMPTE/CCE-CHEM measurements.
722 *Journal of Geophysical Research*, 104(A12), 28615–28624. doi:10.1029/1999JA900310
723
724 Denton, R. E., Gary, S. P., Anderson, B. J., Fuselier, S. A., & Hudson, M. K. (1994), Low-
725 frequency magnetic fluctuation spectra in the magnetosheath and plasma depletion layer. *Journal
726 of Geophysical Research*, 99(A4), 5893–5901. doi:10.1029/93JA02729
727
728 Ebihara, Y., and Miyoshi, Y. (2011), Dynamic Inner Magnetosphere: A Tutorial and Recent
729 Advances. In: Liu W., Fujimoto M. (eds) The Dynamic Magnetosphere. IAGA Special Sopron
730 Book Series, vol 3. Springer, Dordrecht. doi:10.1007/978-94-007-0501-2_9
731
732 Engebretson, M. J., Peterson, W. K., Posch, J. L., Klatt, M. R., Anderson, et al. (2002),
733 Observations of two types of Pc 1-2 pulsations in the outer dayside magnetosphere. *Journal of
734 Geophysical Research*, 107(A12), 1451. doi:10.1029/2001JA000198
735
736 Gary, S. P., & Lee, M. A. (1994), The ion cyclotron anisotropy instability and the inverse
737 correlation between proton anisotropy and proton beta. *Journal of Geophysical Research*, 99,
738 11297–11301. doi:10.1029/94JA00253
739
740 Halford, A. J., Fraser, B. J., & Morley, S. K. (2010), EMIC wave activity during geomagnetic
741 storm and nonstorm periods: CRRES results. *Journal of Geophysical Research*, 115, A12248.
742 doi:10.1029/2010JA015716
743
744 Imajo, S., Nosé, M., Kasahara, S.,Yokota, S., Matsuoka, A., Keika, K.,et al. (2019), Meridional
745 distribution of middle-energy protons and pressure-driven currents in the nightside inner
746 magnetosphere: Arase observations. *Journal of Geophysical Research: Space Physics*, 124,5719–
747 5733. doi:10.1029/2019JA026682
748
749 Imajo, S., Miyoshi, Y., Kazama, Y. et al. (2021), Active auroral arc powered by accelerated
750 electrons from very high altitudes. *Scientific reports*, 11, 1610. doi: 10.1038/s41598-020-79665-5
751
752 Jahn et al., 2017 Jahn, J. M., Goldstein, J., Reeves, G. D., Fernandes, P. A., Skoug, R. M., Larsen,
753 B. A., & Spence, H. E. (2017), The warm plasma composition in the inner magnetosphere during
754 2012–2015. *Journal of Geophysical Research: Space Physics*, 122, 11,018–11,043.
755 doi:10.1002/2017ja024183
756
757 Jordanova, V. K., Albert, J., and Miyoshi, Y. (2008), Relativistic electron precipitation by EMIC
758 waves from self-consistent global simulations, *Journal of Geophysical Research: Space Physics*,
759 113, A00A10. doi:10.1029/2008JA013239
760

761 Jun, C.-W., Yue, C., Bortnik, J., Lyons, L. R., Nishimura, Y., Kletzing, C., Wygant, J., & Spence,
762 H. (2019a), A statistical study of EMIC waves associated with and without energetic particle
763 injection from the magnetotail. *Journal of Geophysical Research: Space Physics*, 124, 1-18.
764 doi:10.1029/2018JA025886
765
766 Jun, C.-W., Yue, C., Bortnik, J., Lyons, L. R., Nishimura, Y. T., & Kletzing, C. A. (2019b), EMIC
767 wave properties associated with and without injections in the inner magnetosphere. *Journal of
768 Geophysical Research: Space Physics*, 124, 2029-2045. doi:10.1029/2018JA026279
769
770 Jun, C.-W., Miyoshi, Y., Kurita, S., Yue, C., Bortnik, J., Lyons, L., et al. (2021), The
771 characteristics of EMIC waves in the magnetosphere based on the Van Allen Probes and Arase
772 observations. *Journal of Geophysical Research: Space Physics*, 126, e2020JA029001.
773 doi:10.1029/2020JA029001
774
775 Kanekal, S., and Miyoshi, Y. (2021), Dynamics of the terrestrial radiation belts: A review of recent
776 results during the VarSITI (Variability of the Sun and Its Terrestrial Impact) era, 2014-2018.
777 *Progress in Earth and Planetary Science*, 8, 35. doi:10.1186/s40645-021-00413-y
778
779 Kasahara, Y., Kasaba, Y., Kojima, H. et al. (2018a), The Plasma Wave Experiment (PWE) on
780 board the Arase (ERG) satellite. *Earth, Planets and Space*, 70, 86. doi:10.1186/s40623-018-0842-
781 4
782
783 Kasahara, Y., et al. (2018b), The PWE/HFA instrument Level-2 spectrum data of Exploration of
784 energization and Radiation in Geospace (ERG) Arase satellite. doi:10.34515/DATA.ERG-10000
785
786 Keika, K., Takahashi, K., Ukhorskiy, A. Y., & Miyoshi, Y. (2013), Global characteristics of
787 electromagnetic ion cyclotron waves: Occurrence rate and its storm dependence. *Journal of
788 Geophysical Research*, 118, 4,135-4,150. doi:10.1002/jgra.50385
789
790 Kim, E.-H., & Johnson, J. R. (2016), Full-wave modeling of EMIC waves near the He^+
791 gyrofrequency. *Geophysical Research Letters*, 43, 13-21. doi:10.1002/2015GL066978
792
793 Kim, G.-J., Kim, K.-H., Lee, D.-H., Kwon, H.-J., and Park, J.-S. (2016b), Occurrence of EMIC
794 waves and plasmaspheric plasmas derived from THEMIS observations in the outer
795 magnetosphere: Revisit. *Journal of Geophysical Research: Space Physics*, 121, 9,443-9,458.
796 doi:10.1002/2016JA023108
797
798 Kozyra, J. U., Cravens, T. E., Nagy, A. F., Fontheim, E. G., and Ong, R. S. B. (1984), Effects of
799 energetic heavy ions on electromagnetic ion cyclotron wave generation in the plasmapause region.
800 *Journal of Geophysical Research: Space Physics*, 89(A4), 2217-2233.
801 doi:10.1029/JA089iA04p02217
802
803 Kumamoto, A., Tsuchiya, F., Kasahara, Y., Kasaba, Y., Kojima, H., Yagitani, S., et al. (2018),
804 High frequency analyzer (HFA) of Plasma Wave Experiment (PWE) onboard the Arase spacecraft.
805 *Earth, Planets and Space*, 70, 82. doi: 10.1186/s40623-018-0854-0
806

807 Kurita, S., Miyoshi, Y., Shiokawa, K., Higashio, N., Mitani, T., et al. (2018), Rapid Loss of
808 Relativistic Electrons by EMIC Waves in the Outer Radiation Belt Observed by Arase, Van Allen
809 Probes, and the PWING Ground Station., *Geophysical Research Letters*, 45, 12720-12729.
810 doi:10.1029/2018GL080262

812 Lee, D.-Y., Noh, S.-J., Choi, C.-R., Lee, J. J., & Hwang, J. A. (2017), Effect of hot anisotropic
813 He$^+$ ions on the growth and damping of electromagnetic ion cyclotron waves in the inner
814 magnetosphere. *Journal of Geophysical Research*, 122, 4,935-4,942. doi:10.1002/2016JA023826

816 Li, W., and Hudson, M. K. (2019), Earth's Van Allen radiation belts: From discovery to the Van
817 Allen Probes era. *Journal of Geophysical Research: Space Physics*, 124, 8319-8351. doi:10.1029/
818 2018JA025940

820 Lin, R. -L., Zhang, J.-C., Allen, R. C., Kistler, L. M., Mouikis, C. G., Gong, J.-C., et al. (2014),
821 Testing linear theory of EMIC waves in the inner magnetosphere: Cluster observations. *Journal
822 of Geophysical Research: Space Physics*, 119, 1004–1027. doi:10.1002/2013JA019541

824 Loto'aniu, T. M., Fraser, B. J., & Waters, C. L. (2005), Propagation of electromagnetic ion
825 cyclotron wave energy in the magnetosphere. *Journal of Geophysical Research*, 110, A07214.
826 doi:10.1029/2004JA010816

828 Ma, Q., Li, W., Yue, C., Thorne, R. M., Bortnik, J., Kletzing, C. A., et al. (2019), Ion heating by
829 electromagnetic ion cyclotron waves and magnetosonic waves in the Earth's inner magnetosphere.
830 *Geophysical Research Letters*, 46. doi:10.1029/2019GL083513

832 Matsuda, S., Kasahara, Y., Miyoshi, Y., Nomura, R., Shoji, M., Matsuoka, A., et al. (2018a),
833 Spatial distribution of fine-structured and unstructured EMIC waves observed by the Arase
834 satellite. *Geophysical Research Letters*, 45, 11,530-11,538. doi:10.1029/2018GL080109

836 Matsuda, S., Kasahara, Y., Kojima, H., Kasaba, Y., Yagitani, S., Ozaki, M., et al. (2018b),
837 Onboard software of Plasma Wave Experiment aboard Arase: Instrument management and signal
838 processing of waveform capture/onboard frequency analyzer. *Earth, Planets and Space*, 70, 75.
839 doi:10.1186/s40623-018-0838-0

841 Matsuda, S., Miyoshi, Y., Kasahara, Y., Blum, L., Colpitts, C., Asamura, K., et al. (2021).
842 Multipoint measurement of fine-structured EMIC waves by Arase, Van Allen Probe A, and ground
843 stations. *Geophysical Research Letters*, 48, e2021GL096488. doi:10.1029/2021GL096488

845 McCollough, J. P., Elkington, S. R., Usanova, M. E., Mann, I. R., Baker, D. N., & Kale, Z. C.
846 (2010), Physical mechanisms of compressional EMIC wave growth. *Journal of Geophysical
847 Research*, 115, A10214. doi:10.1029/2010JA015393

849 Meredith, N. P., Thorne, R. M., Horne, R. B. , Summers, D., Fraser, B. J., & Anderson, R. R.
850 (2003), Statistical analysis of relativistic electron energies for cyclotron resonance with EMIC
851 waves observed on CRRES. *Journal of Geophysical Research*, 108(A6), 1250.
852 doi:10.1029/2002JA009700

853

854 Meredith, N. P., Horne, R. B., Kersten, T., Fraser, B. J., and Grew, R. S. (2014), Global
855 morphology and spectral properties of EMIC waves derived from CRRES observations. *Journal*
856 *of Geophysical Research: Space Physics*, 119, 5,328-5,342. doi:10.1002/2014JA020064

857

858 Min, K., Lee, J., Keika, K., & Li, W. (2012), Global distribution of EMIC waves derived from
859 THEMIS observations. *Journal of Geophysical Research*, 117, A05219.
860 doi:10.1029/2012JA017515

861

862 Min, K., Kim, J., Ma, Q. et al. (2021), Unusual high frequency EMIC waves: Detailed analysis of
863 EMIC wave excitation and energy coupling between EMIC and magnetosonic waves. *Advances*
864 *in Space Research*. doi:10.1016/j.asr.2021.07.039

865

866 Miyoshi, Y., Sakaguchi, K., Shiokawa, K., Evans, D., Albert, J., Connors, M., & Jordanova, V.
867 (2008), Precipitation of radiation belt electrons by EMIC waves, observed from ground and space.
868 *Geophysical Research Letters*, 35, L23101. doi:10.1029/2008GL035727\

869

870 Miyoshi, Y., Shinohara, I., Takashima, T., Asamura, K., Higashio, N., Mitani, T., et al. (2018a),
871 Geospace exploration project ERG. *Earth, Planets and Space*, 70, 101. doi:10.1186/s40623-018-
872 0862-0

873

874 Miyoshi, Y., Hori, T., Shoji, M. et al. (2018b) The ERG Science Center. Earth, Planets, and Space
875 70, 96. doi:10.1186/s40623-018-0867-8

876

877 Miyoshi, Y., Shinohara, I. and Jun, C.-W. (2018c), The Level-2 orbit data of Exploration of
878 energization and Radiation in Geospace (ERG) Arase satellite. doi:10.34515/DATA.ERG-12000

879

880 Miyoshi, Y., Shinohara, I. and Jun, C.-W. (2018d), The Level-3 orbit data of Exploration of
881 energization and Radiation in Geospace (ERG) Arase satellite. doi:10.34515/DATA.ERG-12001

882

883 Miyoshi, Y., Matsuda, S., Kurita, S.,Nomura, K., Keika, K., Shoji, M., et al. (2019), EMIC waves
884 converted from equatorial noise due to M/Q= 2 ions in the plasmasphere: Observations from Van
885 Allen Probes and Arase. *Geophysical Research Letters*, 46, 5662-5669.
886 doi:10.1029/2019GL083024

887

888 Miyoshi, Y., Shinohara, I., Ukhorskiy, S. et al. (2022), Collaborative Research Activities of the
889 Arase and Van Allen Probes, Space Sci Rev, 218, 38. doi:10.1007/s11214-022-00885-4

890

891 Nakamura, S., Y. Omura, S. Machida, M. Shoji, M. Nosé, and V. Angelopoulos (2014),
892 Electromagnetic ion cyclotron rising tone emissions observed by THEMIS probes outside the
893 plasmapause. *Journal of Geophysical Research: Space Physics*, 119, 1,874-1,886.
894 doi:10.1002/2013JA019146

895

896 Nakamura, S., Omura, Y., and Angelopoulos V. (2016), A statistical study of EMIC rising and
897 falling tone emissions observed by THEMIS. *Journal of Geophysical Research: Space*
898 *Physics*,121, 8374-8391. doi:10.1002/2016JA022353

899

900 Noh, S.-J., Lee, D.-Y., Choi, C.-R., Kim, H., & Skoug, R. (2018), Test of ion cyclotron resonance
901 instability using proton distributions obtained from Van Allen Probe-A observations. *Journal of*
902 *Geophysical Research: Space Physics*, 123, 6591–6610. doi:10.1029/2018JA025385

903

904 Ozaki, M., Shiokawa, K., Miyoshi, Y., Kataoka, R., Connors, M., Inoue, T., et al. (2018),
905 Discovery of 1 Hz range modulation of isolated proton aurora at subauroral latitudes. *Geophysical*
906 *Research Letters*, 45(3), 1209–1217. doi:10.1002/2017GL076486

907

908 Ozaki, M., Shiokawa, K., Horne, R. B., Engebretson, M. J., Lessard, M., Ogawa, Y., et al. (2021),
909 Magnetic conjugacy of Pc1 waves and isolated proton precipitation at subauroral latitudes:
910 Importance of ionosphere as intensity modulation region. *Geophysical Research Letters*, 48,
911 e2020GL091384. doi:10.1029/2020GL091384

912

913 Park, J.-S., Kim, K.-H., Shiokawa, K., Lee, D.-H., Lee, E., Kwon, H.-J., Jin, H., & Jee, G. (2016),
914 EMIC waves observed at geosynchronous orbit under quiet geomagnetic conditions (Kp<1).
915 *Journal of Geophysical Research*, 121, 1,377-1,390. doi:10.1002/2015JA021968

916

917 Park, J.-S., Shue, J.-H., & Kim, K.-H. (2017), Dependence of electromagnetic ion cyclotron wave
918 occurrence on north-south orientation of interplanetary magnetic field: THEMIS observations.
919 Journal   of   Geophysical   Research: Space   Physics,   122,   11,354–11,372.
920 doi:10.1002/2017JA024507

921

922 Saikin, A. A., Zhang J.-C., Allen, R. C., Smith, C. W., Kistler, L. M., Spence, H. E., et al. (2015),
923 The occurrence and wave properties of H^+-, He^+-, and O^+-band EMIC waves observed by the Van
924 Allen Probes. *Journal of Geophysical Research: Space Physics*, 120, 7,477-7,492.
925 doi:10.1002/2015JA021358

926

927 Saikin, A. A., Zhang, J.-C., Smith, C. W., Spence, H. E., Torbert, R. B., & Kletzing, C. A. (2016),
928 The dependence on geomagnetic conditions and solar wind dynamic pressure of the spatial
929 distributions of EMIC waves observed by the Van Allen Probes. *Journal of Geophysical Research:*
930 *Space Physics*, 121, 4,362-4,377. doi:10.1002/2016JA022523

931

932 Sakaguchi, K., Shiokawa, K., Ieda, A., Miyoshi, Y., Otsuka, Y., Ogawa, T., Connors, M.,
933 Donovan, E. F., & Rich, F. J. (2007), Simultaneous ground and satellite observations of an isolated
934 proton arc at subauroral latitudes. *Journal of Geophysical Research*, 112, A04202.
935 doi:10.1029/2006JA012135

936

937 Sakaguchi, K., Kasahara, Y., Shoji, M., Omura, Y.,4, et al. (2013), Akebono observations of EMIC
938 waves in the slot region of the radiation belts. *Geophysical Research Letters*, 40, 5587-5591.
939 doi:10.1002/2013GL058258

940

941 Shoji, M., Miyoshi, Y., Omura, Y.,Kistler, L. M., Kasaba, Y., Matsuda, S.,et al. (2018).
942 Instantaneous frequency analysis on nonlinear EMIC emissions: Arase observation. *Geophysical*
943 *Research Letters*, 45, 13,199-13,205. doi:10.1029/2018GL079765

944

945 Shoji, M., Miyoshi, Y., Kistler, L.M. et al (2021), Discovery of proton hill in the phase space
946 during interactions between ions and electromagnetic ion cyclotron waves. Science Report, 11,
947 13480. doi:10.1038/s41598-021-92541-0

948

949 Shumko, M. B. Gallardo-Lacourt, A. J. Halford, L. W. Blum, J. Liang et al. (2022), Proton Aurora
950 and Relativistic Electron Microbursts Scattered by EMIC Waves, Front. Astron. Space Sci.,
951 9:975123. doi;10.3389/fspas.2022.975123

952

953 Stix, T. H. (1962), The Theory of Plasma Waves, McGraw-Hill, New York.

954

955 Teng, S., Li, W., Tao, X., Ma, Q., Wu, Y., Capannolo, L., et al. (2019), Generation and
956 characteristics of unusual high frequency EMIC waves. *Geophysical Research Letters*, 46, 14,230-
957 14,238. doi:10.1029/2019GL085220

958

959 Thorne, R. M. (2010), Radiation belt dynamics: The importance of wave-particle interactions.
960 *Geophysical Research Letters*, 37, L22107. doi:10.1029/2010GL044990

961

962 Tsurutani, B. T., et al. (2016), Heliospheric Plasma Sheet (HPS) impingement onto the
963 magnetosphere as a cause of Relativistic Electron Dropouts (REDs) via coherent EMIC wave
964 scattering with possible consequences for climate change mechanisms. *Journal of Geophysical*
965 *Research: Space Physics*, 121, 10,130-10,156. doi:10.1002/2016JA022499

966

967 Tsyganenko, N. A., and Sitnov, M. I. (2005), Modeling the dynamics of the inner magnetosphere
968 during strong geomagnetic storms. *Journal of Geophysical Research*, 110, A03208.
969 doi:10.1029/2004JA010798

970

971 Usanova, M. E., Mann, I. R., Rae, I. J., Kale, Z. C., Angelopoulos, V., Bonnell, J. W., et al.(2008),
972 Multipoint observations of magnetospheric compression-related EMIC Pc1 waves by THEMIS
973 and CARISMA. *Geophysical Research Letters*, 35, L17S25. doi: 10.1029/2008GL034458

974

975 Usanova, M. E., Mann, I. R., Bortnik, J., Shao, L., and Angelopoulos, V. (2012), THEMIS
976 observations of electromagnetic ion cyclotron wave occurrence: Dependence on AE, SYMH, and
977 solar wind dynamic pressure. *Journal of Geophysical Research*, 117, A10218.
978 doi:10.1029/2012JA018049

979

980 Vines, S. K., Allen, R. C., Anderson, B. J., Engebretson, M. J., Fuselier, S. A., Russell, C. T., et
981 al. (2019), EMIC waves in the outer magnetosphere: Observations of an off-equator source region.
982 *Geophysical Research Letters*, 46, 5,707-5,716. doi:10.1029/ 2019GL082152

983

984 Wang, D., et al. (2015), Statistical characteristics of EMIC waves: Van Allen Probe observations.
985 *Journal of Geophysical Research: Space Physics*, 120, 4,400-4,408. doi:10.1002/2015JA021089

986

987 Wang, D., et al. (2016), Geomagnetic storms and EMIC waves: Van Allen Probe observations.
988 *Journal of Geophysical Research: Space Physics*, 121, 6444- 6457. doi:10.1002/2015JA022318.

989

990   Wang, X. Y., et al. (2017), The occurrence and wave properties of EMIC waves observed by the
991   Magnetospheric Multiscale (MMS) mission. *Journal of Geophysical Research: Space Physics*,
992   122, 8,228-8,240. doi:10.1002/2017JA024237

994   Yokota, S., Kasahara, S., Mitani, T. et al. (2017), Medium-energy particle experiments–ion mass
995   analyzer (MEP-i) onboard ERG (Arase). *Earth Planets Space*, 69, 172. doi.10.1186/s40623-017-
996   0754-8

998   Yue, C., Zong, Q.-G., & Wang, Y. F. (2009), Response of the magnetic field and plasmas at the
999   geosynchronous orbit to interplanetary shock. *Chinese Science Bulletin*, 54. doi: 10.1007/s11434-
1000   009-0649-6

1002   Yue, C., Zong, Q.-G., Zhang, H., Wang, Y. F., Yuan, C. J., Pu, Z. Y., et al. (2010), Geomagnetic
1003   activities triggered by interplanetary shocks. *Journal of Geophysical Research: Space Physics*,
1004   115, A00I05. doi:10.1029/2010JA015356

1006   Yue, C., Zong, Q., Wang, Y., Vogiatzis, I. I., Pu, Z., Fu, S., & Shi, Q. (2011), Inner magnetosphere
1007   plasma characteristics in response to interplanetary shock impacts. *Journal of Geophysical
1008   Research: Space Physics*, 116, A11206. doi:10.1029/2011JA016736

1010   Yue, C., Bortnik, J., Chen, L., Ma, Q., Thorne, R. M., Reeves, G. D., & Spence, H. E. (2017a),
1011   Transitional behavior of different energy protons based on Van Allen Probes observations.
1012   *Geophysical Research Letters*, 44(2), 625-633. doi:10.1002/2016GL071324

1014   Yue, C., Bortnik, J., Thorne, R. M., Ma, Q., An, X., Chappell, C. R., et al. (2017b), The
1015   characteristic pitch angle distributions of 1 eV to 600 keV protons near the equator based on Van
1016   Allen Probes observations. *Journal of Geophysical Research: Space Physics*, 122, 9,464-9,473.
1017   doi.org/10.1002/2017JA024421

1019   Yue, C., Bortnik, J., Li, W., Ma, Q., Gkioulidou, M., Reeves, G. D., et al. (2018), The composition
1020   of plasma inside geostationary orbit based on Van Allen Probes observations. *Journal of
1021   Geophysical Research: Space Physics*, 123, 6,478-6,493. doi:10.1029/2018JA025344

1023   Yue, C., Jun, C.-W., Bortnik, J., An, X., Ma, Q., Reeves, G. D., et al. (2019), The relationship
1024   between EMIC wave properties and proton distributions based on Van Allen probes observations.
1025   *Geophysical Research Letters*, 46, 4,070-4,078. doi:10.1029/2019GL082633

1027   Zhou, X, and Tsurutan, B. T. (1999), Rapid intensification and propagation of the dayside aurora:
1028   Large scale interplanetary pressure pulses (fast shocks) . *Geophysical Research Letters*, 26(8),
1029   1097-1100. doi:10.1029/1999GL900173
1030